A Dual Hollow-core Negative Curvature Fiber Polarization Beam Splitter Covering the O+E+S+C+L Communication Band

YUETING NI,[1] JINHUI YUAN,[1,2,6] SHI QIU,[1] GUIYAO ZHOU,[3,7] CHANGMING XIA,[3] XIAN ZHOU,[2] BINBIN YAN,[1] QIANG WU,[4,5] KUIRU WANG,[1] XINZHU SANG,[1] AND CHONGXIU YU[1]

[1]*State Key Laboratory of Information Photonics and Optical Communications, Beijing University of Posts and Telecommunications, Beijing 100876, China*
[2]*Research Center for Convergence Networks and Ubiquitous Services, University of Science & Technology Beijing, Beijing 100083, China*
[3]*Guangdong Province Key Laboratory of Nano-Photonic Functional Materials and Devices, South China Normal University, Guangzhou, 510006, China*
[4]*Department of Physics and Electrical Engineering, Northumbria University, Newcastle upon Tyne, NE1 8ST, United Kingdom*
[5]*Key Laboratory of Nondestructive Test (Ministry of Education), Nanchang Hong Kong University, Nanchang 330063, China*
[6]*yuanjinhui81@bupt.edu.cn*
[7]*gyzhou@scnu.edu.cn*

Abstract: In this paper, a dual hollow-core negative curvature fiber is proposed for the polarization beam splitter. The effects of the structure parameters of the dual hollow-core negative curvature fiber on the coupling length and coupling length ratio of the *x*-polarized and *y*-polarized core modes and the higher-order mode extinction ratio are analyzed by the finite element method. Moreover, the normalized output powers of the *x*-polarized and *y*-polarized modes in the cores A and B and the corresponding extinction ratio are also investigated by the mode coupling theory. The simulation results show that the dual hollow-core negative curvature fiber polarization beam splitter with the length of 6.45 cm can achieve a broad bandwidth of 400 nm (1.23-1.63 μm), covering the O+E+S+C+L communication band. Besides, the higher-order mode extinction ratio is greater than 100 in the considered wavelength range, which means that it has good single-mode characteristics. It is believed that the proposed dual hollow-core negative curvature fiber polarization beam splitter will have significant application in the optical communication system.

1. Introduction

As an important passive optoelectronic device, the optical fiber polarization beam splitter (PBS), which can split a beam of light into two beams of orthogonal linearly polarized beams, has a wide range of applications in the optical communication system and other fields [1-6]. For the optical fiber PBS, its length is relatively long due to the small birefringence, along with the narrow bandwidth. Photonic crystal fibers (PCFs) have broken through the bottleneck of the traditional optical fibers by relying on the geometric structure-induced unique optical properties, providing new opportunities for the design of the PBS [7-11].

In 2016, Wang *et al.* proposed a square lattice PCF PBS with the two elliptic air holes, where the PBS length was 93.3 μm and the bandwidth was about 70 nm [12]. In 2018, Wang *et al.* designed a liquid-filled dual-core PCF PBS, whose length was only 78 μm and extinction ratio could reach 87 dB at wavelength 1.55 μm [13]. In 2019, Rahman *et al.* demonstrated a gold-filled PCF PBS based on the surface plasmon resonance (SPR) effect, where the PBS length was only 57 μm and the bandwidth was up to 530 nm, covering all the

communication bands [14]. The previous reported works are based on the solid-core PCFs. For the solid-core PCFs, the absorption loss of the substrate material has the adverse effect on the PBS performance. In addition, in order to improve the birefringence of the solid-core PCFs, the elliptical holes, liquid filling, and gold filling are usually used, which make the fabrication process complex and increase the costs.

The hollow-core negative curvature fibers (HC-NCFs) can make the light energy propagated in the air core due to the anti-resonant structure [15-18], which makes it have the low propagation loss [19], low dispersion [20], and low nonlinearity [21]. In recent years, the HC-NCFs are widely used in the fiber sensing [22], high power pulse transmission [23], supercontinuum generation [24] and other fields [25-28]. The application of the HC-NCFs in the PBS has also been reported. In 2019, Zhao *et al.* proposed a dual hollow-core NCF (DHC-NCF) PBS with two elliptical tubes, where it had the length of 6.75 cm and the bandwidth of 310 nm (1.41 to 1.72 μm) [29]. In 2021, Jia *et al.* reported a DHC-NCF PBS with the length of 4.42 cm and the bandwidth of 460 nm (1.4 to 1.86 μm) [30]. In 2021, Jia *et al*. designed a single-mode PBS based on the DHC-NCF with two elliptical tubes nested with the circular tubes, where the PBS length was 8.15 cm and the bandwidth was 370 nm (1.28 to 1.65 μm) [31]. In 2022, Shaha *et al*. demonstrated a short-length DHC-NCF with two elliptical tubes splitting the two cores, where the bandwidth covered the wavelength range from 1.285 to 1.625 μm [32]. In the previous works, the reported DHC-NCF PBSs cannot cover the shorter wavelength range, such as the O and E bands. In addition, the fabrications of them are difficult due to the introduction of the elliptical tubes.

In this paper, a DHC-NCF PBS is proposed. Two silica tubes are introduced to separate the core region into the two symmetrical cores A and B. The coupling length (*CL*), coupling length ratio (*CLR*), and higher-order mode extinction ratio (HOMER) are analyzed. The normalized output powers of the *x*-polarized (*x*-pol) and *y*-polarized (*y*-pol) modes in the cores A and B and polarization extinction ratio (*ER*) are also investigated. The simulation results show that the proposed DHC-NCF PBS achieve a broad bandwidth of 400 nm, covering the O+E+S+C+L communication band, and has good single-mode characteristics.

2. The DHC-NCF PBS structure and theory

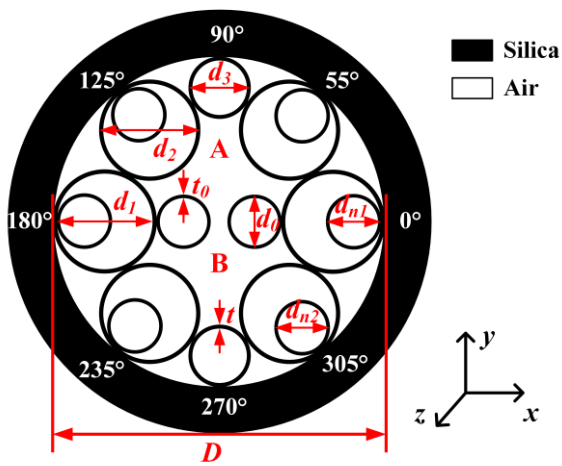

Fig. 1. The cross-sectional structure of the designed DHC-NCF PBS.

Fig. 1 shows the cross-sectional structure of the designed DHC-NCF PBS. From Fig. 1, the core region is composed of two silica tubes, and the diameter and thickness of the silica tubes are set as d_0 and t_0, respectively. The two cores A and B are separated by the two silica tubes. The cladding region of the DHC-NCF is composed of eight silica tubes, which are arranged

at different angles around the center point. The diameter of the two outer silica tubes in the horizontal direction (0° and 180°) is set as d_1, the diameter of the silica tubes in the vertical direction (90° and 270°) is set as d_3, and the diameter of the silica tubes at the four corners (55°, 125°, 235°, and 305°) is set as d_2. The ratio of the nested silica tube and outer tube diameter is k, i.e. $d_{ni} = k*d_i$ (i = 1, 2). The thickness of all eight silica tubes in the cladding region is set as t, and the diameter of the DHC-NCF is set as D. The eight silica tubes of the outer cladding are connected to each other. Two silica tubes with the diameter d_0 are connected to the two ones with the diameter d_1. The width of the gap between the two silica tubes with the diameter d_0 can be calculated by D, d_1, and d_0. The initial structure parameters of the proposed DHC-NCF are set as following: d_1 = 20 μm, d_2 = 18.3 μm, d_3 = 9.8 μm, t = 0.5 μm, d_0 = 9 μm, t_0 = 0.5 μm, k = 0.5, and D = 60 μm. The propagation characteristic of the DHC-NCF can be calculated by the finite element method (FEM). The perfect match layer (PML) is added at the outside of the DHC-NCF, whose thickness and refractive index are chosen as 15 μm and n_{silica}+0.03, respectively. Besides, the grid size of the silica is set as $\lambda/5$, and the grid sizes of the PML and air are set as $\lambda/4$.

The material dispersion of the silica can be obtained from the following Sellmeier equation [33]

$$n_{\mathrm{Silica}}(\lambda) = \sqrt{1 + \frac{\mathrm{A}_1 \lambda^2}{\lambda^2 - \mathrm{B}_1^2} + \frac{\mathrm{A}_2 \lambda^2}{\lambda^2 - \mathrm{B}_2^2} + \frac{\mathrm{A}_3 \lambda^2}{\lambda^2 - \mathrm{B}_3^2}}, \tag{1}$$

where A_1 = 0.6961663, A_2 = 0.4079426, A_3 = 0.897479, B_1 = 0.00684043, B_2 = 0.1162414, B_3 = 9.896161, and λ is the free space wavelength in micrometer.

The coupling lengths CL_{X} and CL_{Y} of the x-pol and y-pol core modes can be obtained by [34]

$$CL_{\mathrm{X}} = \frac{\lambda}{2\left|(n_{\mathrm{even}}^{\mathrm{X}} - n_{\mathrm{odd}}^{\mathrm{X}})\right|}, \tag{2}$$

$$CL_{\mathrm{Y}} = \frac{\lambda}{2\left|(n_{\mathrm{even}}^{\mathrm{Y}} - n_{\mathrm{odd}}^{\mathrm{Y}})\right|}, \tag{3}$$

where $n_{\mathrm{even}}^{\mathrm{X}}$, $n_{\mathrm{odd}}^{\mathrm{X}}$, $n_{\mathrm{even}}^{\mathrm{Y}}$, and $n_{\mathrm{odd}}^{\mathrm{Y}}$ represent the effective indices of the x-pol even and odd modes and y-pol even and odd modes, respectively.

The coupling length ratio (CLR) can be obtained by [35]

$$CLR = \frac{CL_{\mathrm{Y}}}{CL_{\mathrm{X}}}, \tag{4}$$

where the CLR should be approximately equal to 2 or 1/2 to make the PBS length shorter.

The HOMER can be used to describe the single-mode characteristics of an optical fiber, and it is defined as the ratio of the confinement loss of the higher-order modes (such as LP_{11}) and the confinement loss of the fundamental mode (LP_{01}) [36]

$$\mathrm{HOMER} = \frac{\text{Confinement loss of } \mathrm{LP}_{11}}{\text{Confinement loss of } \mathrm{LP}_{01}}. \tag{5}$$

When the light is incident into the core A, the normalized output powers of the x-pol and y-pol modes in the cores A and B can be described by [37]

$$P_{\mathrm{out,A}}^{\mathrm{X,Y}} = P_{\mathrm{in}} \cos^2\left(\frac{\pi}{2} \frac{L_{\mathrm{P}}}{CL_{\mathrm{X,Y}}}\right), \tag{6}$$

$$P_{\mathrm{out,B}}^{\mathrm{X,Y}} = P_{\mathrm{in}} \sin^2\left(\frac{\pi}{2} \frac{L_{\mathrm{P}}}{CL_{\mathrm{X,Y}}}\right). \tag{7}$$

The ER, which is an important parameter to evaluate the performance of the PBS, can be

described for the core A by [38]

$$ER = 10\log_{10}\frac{P^{X}_{\text{out, A}}}{P^{Y}_{\text{out, A}}}. \quad \textbf{(8)}$$

The polarization beam splitting is possible when the *ER* is below -20 dB. Therefore, the wavelength range below -20 dB is considered as the bandwidth of the PBS. Because the two cores A and B of the DHC-NCF have the same structure, we only need to consider the variations of P_{out} along the *x*-pol and *y*-pol directions and the *ER* in the core A or B when the light is injected into one of the two cores.

3. Simulation results and discussion

According to the mode coupling theory [39], the proposed DHC-NCF could generate the four super modes, which are called as the *x*-pol even mode, *x*-pol odd mode, *y*-pol even mode, and *y*-pol odd mode, respectively. Because of the different propagation constants of the even and odd modes, the *x*-pol and *y*-pol lights will be transferred periodically between the two cores. In order to ensure that the two beams of orthogonally polarized light are well separated within a short coupling length, the birefringence properties of the DHC-NCF need to be enhanced. Therefore, we reduce the size of the vertical tubes, increase the size of the tubes on both sides of the core region, and introduce the nested tubes in the horizontal tubes. At the same time, the introduction of the nested tubes can also reduce the loss of the fundamental mode and increase the HOMER.

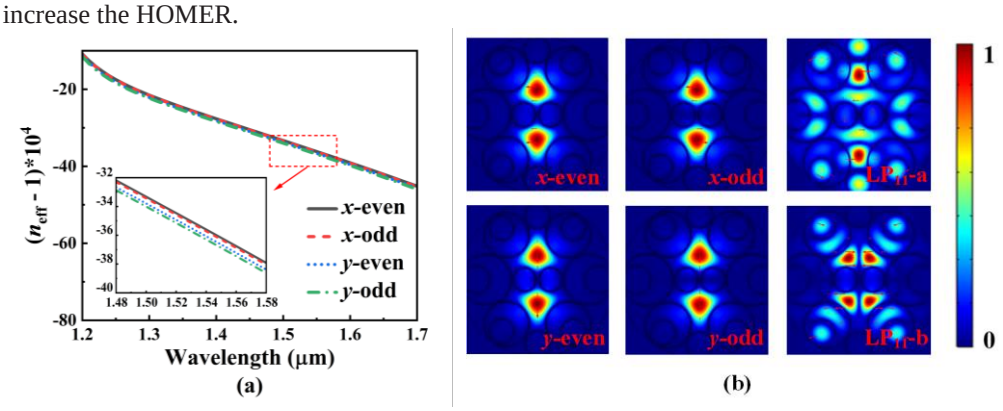

Fig. 2. (a) Effective refractive indices of the *x*-pol and *y*-pol even and odd modes, and (b) the mode field distributions of the *x*-pol and *y*-pol even and odd modes and LP_{11} modes calculated at wavelength 1.55 μm.

The effective refractive indices of the considered four super modes are shown in Fig. 2(a), where the inset shows the zoom-in view within the wavelength range from 1.48 to 1.58 μm. From Fig. 2(a) and the inset, the effective refractive indices of the *x*-pol even and odd modes are larger than those of the *y*-pol even and odd modes, and the effective refractive indices of the *x*-pol and *y*-pol even modes are larger than those of the *x*-pol and *y*-pol odd modes. In the considered wavelength range of 1.48 to 1.58 μm, the *x*-pol even mode has the highest effective refractive index, and the *y*-pol odd mode has the lowest effective refractive index. The effective refractive index difference between the *y*-pol even and odd modes is larger than that of the *x*-pol even and odd modes, which makes the CL_Y of the *y*-pol core modes smaller than the CL_X of the *x*-pol core modes. Fig. 2(b) shows the mode field distributions of the four super modes and two lowest loss higher-order modes (LP_{11} modes) calculated at wavelength 1.55 μm. It can be seen from Fig. 2(b) that the super mode field energies are well confined in the two cores. And some of the energy of the LP_{11} modes is coupled into the silica tubes, which will enhance the HOMER and make the DHC-NCF achieve the better single-mode characteristics.

Based on the initial structure parameters of the proposed DHC-NCF PBS, the calculated CL_X and CL_Y of the *x*-pol and *y*-pol core modes and *CLR* in the wavelength range from 1.30 to 1.70 μm are shown in Fig. 3. Because the two cores and coupling channels are distributed along the *y*-pol direction, the CL_X of the *x*-pol core mode is larger than the CL_Y of the *y*-pol core mode, as seen from Fig. 3. This makes the *y*-pol core modes easier to couple from one core to the other one than the *x*-pol core modes. The CL_X and CL_Y of the *x*-pol and *y*-pol core modes simultaneously increase first and then decrease with the increasing wavelength, reaching a maximum at wavelength 1.48 μm. Thus, the coupling length ratio remains relatively stable around 0.7. In order to obtain the *CLR* of ~ 0.5, the structure parameters of the proposed DHC-NCF PBS need to be optimized. In the following simulation, the working wavelength is set at 1.55 μm.

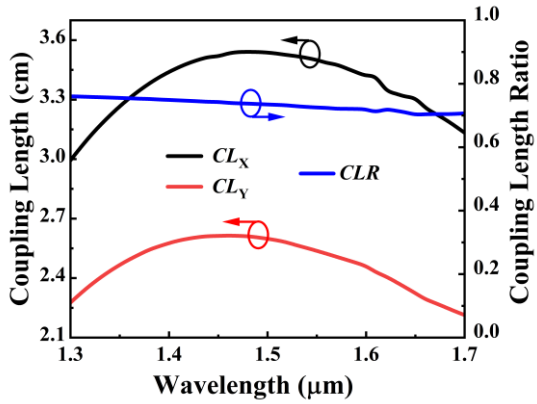

Fig. 3. The CL_X and CL_Y of the *x*-pol and *y*-pol core modes and *CLR* of the DHC-NCF PBS.

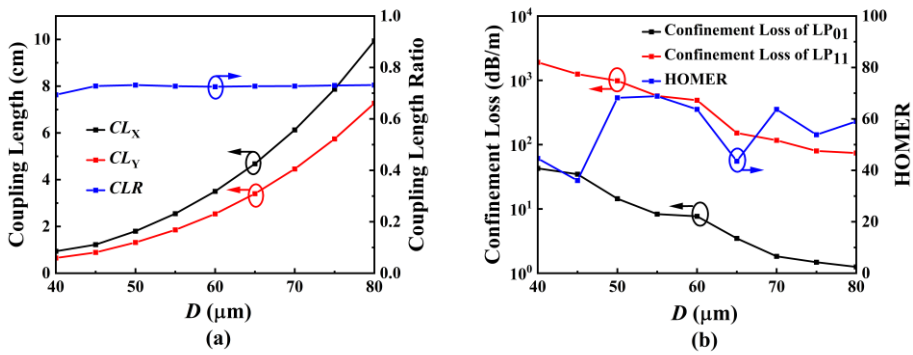

Fig. 4. (a) The CL_X and CL_Y of the *x*-pol and *y*-pol core modes and *CLR*, and (b) the confinement losses of the modes LP_{01} and LP_{11} and HOMER when *D* increases from 40 to 80 μm.

Figs. 4(a) and 4(b) show the CL_X and CL_Y of the *x*-pol and *y*-pol core modes and *CLR* and the confinement losses of the modes LP_{01} and LP_{11} and HOMER, respectively, when *D* increases from 40 to 80 μm. From Fig. 4(a), the CL_X and CL_Y increase significantly with the increase of *D* from 40 to 80 μm. Moreover, as *D* increases, the effective refractive indices of the considered four super modes increase. The effective refractive index differences between the *x*-pol and *y*-pol odd and even modes will decrease significantly, so the CL_X and CL_Y of the *x*-pol and *y*-pol odd and even modes will increase. Since the CL_X and CL_Y increase proportionally, the change of the *CLR* is very small. From Fig. 4(b), as *D* increases, the confinement losses of the higher-order and fundamental modes decrease, and the

corresponding HOMER changes with a certain degree of fluctuation. By the comprehensive consideration of the decreased confinement loss and the increased coupling length of the DHC-NCF PBS, the value of D should be chosen appropriately.

Fig. 5(a) shows the CL_X and CL_Y of the x-pol and y-pol core modes and CLR when t increases from 0.44 to 0.64 μm. According to the resonant condition $\lambda = 2t(n_2 - n_1)^{1/2}/m$ (m = 1,2,…), the increase of t will result in a red-shift of the resonant wavelength. From Fig. 5(a), as t increases from 0.44 to 0.64 μm, the CL_X of the x-pol core mode increases from 3.2 to 4.7 cm, while the CL_Y of the y-pol core mode increases from 2.4 to 2.8 cm. As a result, the CLR decreases from 0.75 to 0.55. Fig. 5(b) shows the relationships between the confinement losses of the modes LP_{01} and LP_{11}, HOMER and t. From Fig. 5(b), the confinement losses of the modes LP_{01} and LP_{11} both decrease first and then increase as t increases. When t is equal to 0.56, the confinement loss of the mode LP_{01} has the lowest value, and the HOMER is larger than 100. Besides, when t is chosen as 0.56 μm, the resonant wavelength is located at 1.16 μm (m = 1). According to the principle of the anti-resonant reflection, the confinement loss of the mode LP_{01} at the resonant wavelength is higher, and thus the working bandwidth of the DHC-NCF PBS should be avoided near the resonant wavelength.

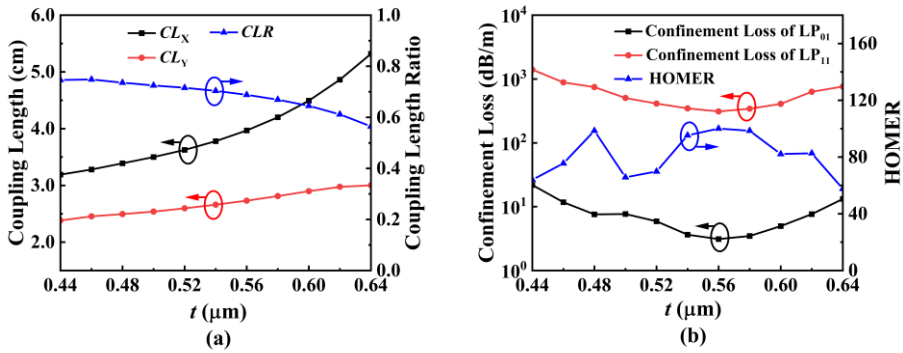

Fig. 5. (a) The CL_X and CL_Y of the x-pol and y-pol core modes and CLR, and (b) the confinement losses of the LP_{01} and LP_{11} and HOMER when t increases from 0.44 to 0.64 μm.

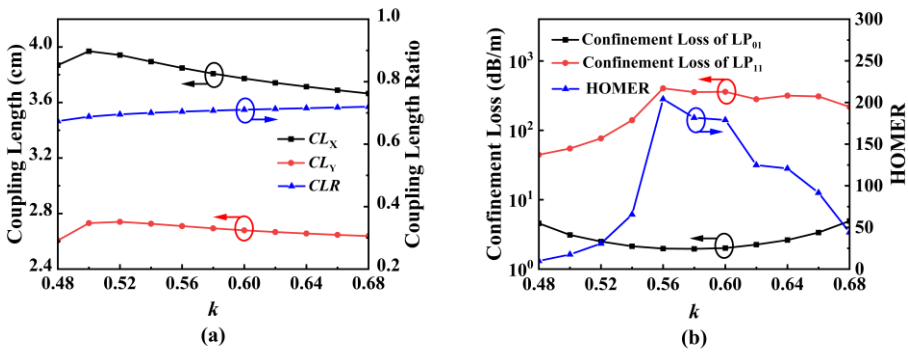

Fig. 6. (a) The CL_X and CL_Y of the x-pol and y-pol core modes and CLR, and (b) the confinement losses of the modes LP_{01} and LP_{11} and HOMER when k increases from 0.48 to 0.68.

Fig. 6(a) shows the CL_X and CL_Y of the x-pol and y-pol core modes and CLR when k increases from 0.48 to 0.68. From Fig. 6(a), as k increases from 0.5 to 0.68, the CL_X and CL_Y of the x-pol and y-pol core modes decrease by a small margin simultaneously. As a result, the CLR increases slightly. Fig. 6(b) shows the relationships between the confinement losses of the modes LP_{01} and LP_{11}, HOMER and k. From Fig. 6(b), as k increases from 0.48 to 0.68,

the confinement loss of the mode LP_{11} first increases and then decreases, while the confinement loss of the mode LP_{01} first decreases and then increases. When k is equal to 0.56, the confinement loss of the mode LP_{11} achieves the maximum value, while the confinement loss of the mode LP_{01} is kept at a lower value. Therefore, the HOMER is larger than 200. As shown in Fig. 1, the nested tubes exist only inside the six silica tubes in the cladding region. Although the sizes of the nested tubes have less effect on the mode coupling between the two cores, they have significant effect on the confinement losses of the modes LP_{01} and LP_{11} and HOMER.

Fig. 7(a) shows the effects of d_1 on the CL_X and CL_Y of the x-pol and y-pol core modes and the CLR at wavelength 1.55 μm. Since the eight silica tubes in the cladding region are closely spaced, the size of d_2 is dependent of the sizes of d_1 and d_3. The decrease of d_2 will lead to the increases of the two core regions, so the relative mode field also increases. When the coupling channel width remains unchanged, the CL_X and CL_Y of the x-pol and y-pol core modes will increase. From Fig. 7(a), as d_1 increases from 19.5 to 21.5 μm, the CL_X and CL_Y of the x-pol and y-pol core modes are growing in the same trend, and the CLR remains almost constant. Thus, the variation of d_1 has less effect on the CLR. Fig. 7(b) shows the relationships between the confinement losses of the modes LP_{01} and LP_{11}, HOMER and d_1. From Fig. 7(b), the confinement losses of the modes LP_{01} and LP_{11} change slightly as d_1 increases. The position of the silica tubes with the size of d_1 is relatively far away from the two cores, so the effect of d_1 on the confinement loss is smaller. When d_1 increases from 19.5 to 21.5 μm, the HOMER is larger than 200, and can be up to 360 when d_1 is chosen as 20.3 μm.

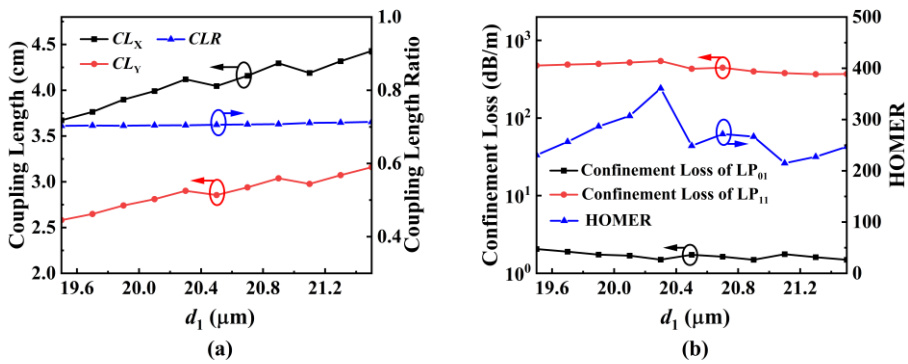

Fig. 7. (a) The CL_X and CL_Y of the x-pol and y-pol core modes and CLR, and (b) the confinement losses of the modes LP_{01} and LP_{11} and HOMER when d_1 increases from 19.5 to 21.5 μm.

The effects of d_3 on the CL_X and CL_Y of the x-pol and y-pol core modes and the CLR are shown in Fig. 8(a). From Fig. 8(a), as d_3 increases, the CL_X and CL_Y of the x-pol and y-pol core modes increase simultaneously, and the CLR remains nearly unchanged. When d_3 increases from 9.5 to 11.5 μm, the CL_X and CL_Y of the x-pol and y-pol core modes increase from 3.6 to 7.3 cm and from 2.5 to 5.3 cm, respectively. And the CLR slightly decreases from 0.73 to 0.71. The increase of d_3 leads to the decrease of d_2, which will increase the mode field area and the coupling length. The relationships between the confinement losses of the modes LP_{01} and LP_{11}, HOMER and d_3 are shown in Fig. 8(b). From Fig. 8(b), as d_3 increases, the confinement loss of the mode LP_{01} first decreases and then increases, and the confinement loss of the mode LP_{11} first increases and then decreases. When d_3 is equal to 10.5 μm, the confinement loss of the mode LP_{01} is close to 1 dB/m, while the confinement loss of the mode LP_{11} is higher than 1000 dB/m. Therefore, the HOMER increases first and then decreases as d_3 increases from 9.5 to 11.5 μm, and reaches the maximum value of 2500 for d_3 of 10.5 μm.

The two silica tubes in the middle and the gap between the two silica tubes form the coupling channel for the two cores. It can be known that t_0 and d_0 have significant effects on the CL_X and CL_Y of the *x*-pol and *y*-pol core modes and the *CLR*. The effects of t_0 on the CL_X and CL_Y of the *x*-pol and *y*-pol core modes and the *CLR* are shown in Fig. 9(a). From Fig. 9(a), the CL_X and CL_Y of the *x*-pol and *y*-pol core modes decrease and the *CLR* increases gradually as t_0 increases. When t_0 decreases from 0.48 to 0.58 μm, the CL_X and CL_Y of the *x*-pol and *y*-pol core modes decrease from 5.7 to 3 cm and from 4 to 2.3 cm, respectively. And the *CLR* increases from 0.7 to 0.76. Fig. 9(b) shows the relationships between the confinement losses of the modes LP_{01} and LP_{11}, HOMER and t_0. From Fig. 9(b), as t_0 increases, the confinement loss of the mode LP_{01} does not change significantly and remains around 1 dB/m, and the confinement loss of the mode LP_{11} also changes little and remains above 1000 dB/m. And the HOMER is larger than 1500 in the t_0 range of 0.49 to 0.57 μm. It indicates that t_0 has little effect on the confinement loss of the core modes.

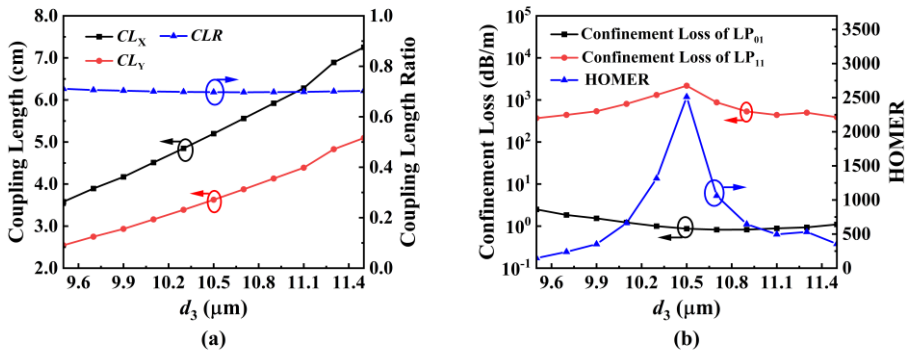

Fig. 8. (a) The CL_X and CL_Y of the *x*-pol and *y*-pol core modes and *CLR*, and (b) the confinement losses of the modes LP_{01} and LP_{11} and HOMER when d_3 increases from 9.5 to 11.5 μm.

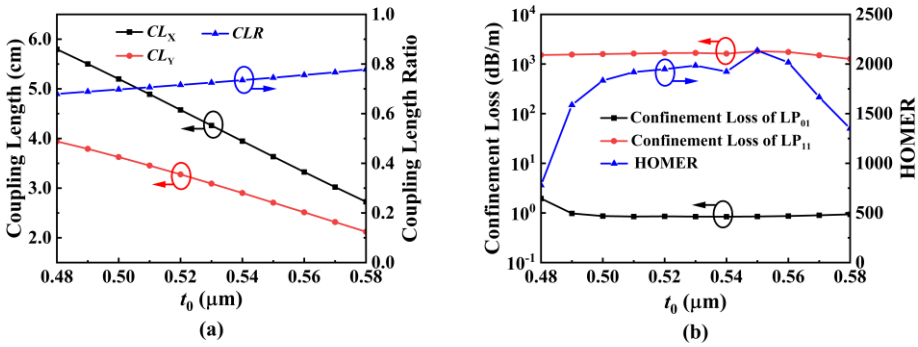

Fig. 9. (a) The CL_X and CL_Y of the *x*-pol and *y*-pol core modes and *CLR*, and (b) the confinement losses of the modes LP_{01} and LP_{11} and HOMER when t_0 increases from 19.5 to 21.5 μm.

Fig. 10(a) shows the CL_X and CL_Y of the *x*-pol and *y*-pol core modes and the *CLR* when d_0 increases. From Fig. 10(a), as d_0 increases from 8.6 to 9.6 μm, the CL_X of the *x*-pol core mode increases significantly from 3.7 to 6.4 cm. In contrast, the variation of the CL_Y of the *y*-pol core mode is relatively gentle, the CL_Y of the *y*-pol core mode has a bulge in the middle, changing within the range of 3.2 to 3.5 cm. And the *CLR* decreases from 0.85 to 0.53. The main reason is considered that the increase of d_0 makes the coupling channel in the *x*-pol direction narrower, so it is more difficult for the *x*-pol core mode to be coupled from one core

to the other one, while the *y*-pol core mode is not significantly affected. Fig. 10(b) shows the relationships between the confinement losses of the modes LP_{01} and LP_{11}, HOMER and d_0. From Fig. 10(b), as d_0 increases from 8.6 to 9.6 μm, the confinement loss of the mode LP_{01} is above and below 1 dB/m, and the confinement loss of the mode LP_{11} is always around 1000 dB/m. And the HOMER can be up to 500 in the d_0 range of 8.6 to 9.6 μm.

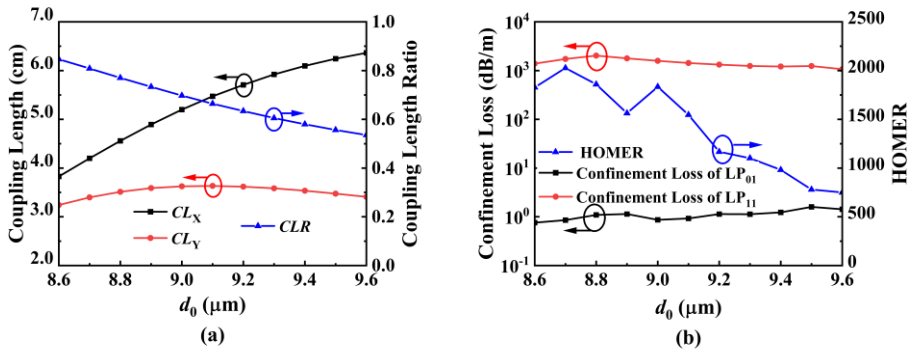

Fig. 10. (a) The CL_X and CL_Y of the *x*-pol and *y*-pol core modes and *CLR*, and (b) the confinement losses of the modes LP_{01} and LP_{11} and HOMER when d_0 increases from 8.6 to 9.6 μm.

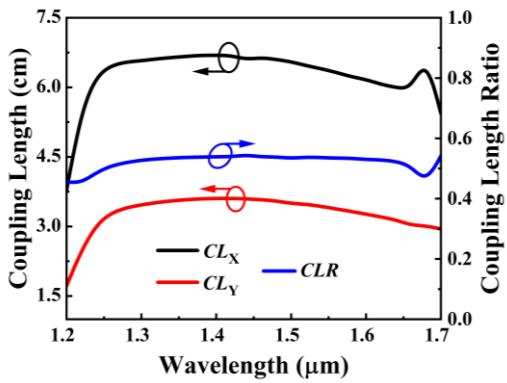

Fig. 11. The CL_X and CL_Y of the *x*-pol and *y*-pol core modes and *CLR* in the wavelength range of 1.2 to 1.7 μm.

Based on the above results, the structure parameters of the DHC-NCF PBS have different effects. Thus, the optimized structure parameters are chosen as following: t = 0.56 μm, k = 0.56, d_1 = 20.3 μm, d_2 = 18.1 μm, d_3 = 10.5 μm, d_0 = 9.6 μm, t_0 = 0.5 μm, and D = 60.6 μm. At this time, the corresponding CL_X and CL_Y of the *x*-pol and *y*-pol core modes and the *CLR* in the wavelength of 1.20 to 1.70 μm are shown in Fig. 11. From Fig. 11, the CL_X and CL_Y of the *x*-pol and *y*-pol core modes change little in the wavelength range of 1.25 to 1.60 μm, and increase simultaneously in the wavelength range of 1.2 to 1.25 μm. In the wavelength range of 1.65 to 1.7 μm, the CL_X of the *x*-pol core mode increases and then decreases, and the CL_Y of the *y*-pol core mode decreases slightly. Therefore, the variation of the *CLR* remains flat in the wavelength range of 1.20 to 1.70 μm, and the *CLR* value changes within the range of 0.45 to 0.54. Because the CL_X and CL_Y of the *x*-pol and *y*-pol core modes and the *CLR* only occur to change slightly within a certain wavelength range, the DHC-NCF PBS could be expected to have a broad bandwidth.

Assuming that the input light at wavelength 1.55 μm being launched into the core A, the normalized output powers of the cores A and B as functions of the propagation distance are

shown in Fig. 12. From Fig. 12, when the propagation distance reaches 6.45 cm, the normalized output power of the *x*-pol light in the core A decreases to 0, but the normalized output power of the *y*-pol light in the core A is almost at its maximum. In the core B, the normalized output power of the *x*-pol light reaches a maximum, and the normalized output power of the *y*-pol light becomes 0 when the propagation distance is 6.45 cm. At this time, the *x*-pol light only exists in the core B, and the *y*-pol light only exists in the core A, which indicates that the *x*-pol and *y*-pol lights are well separated into the cores A and B.

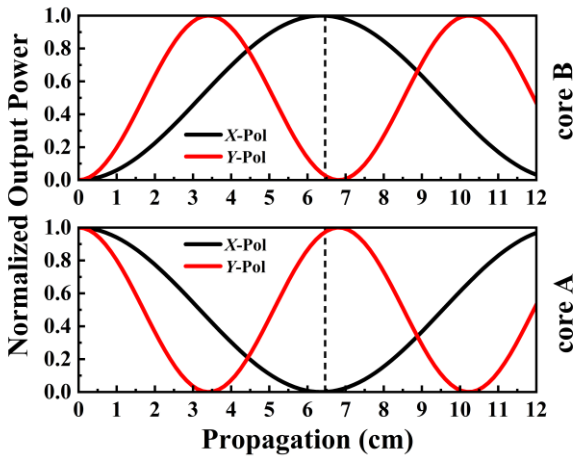

Fig. 12. The normalized output powers of the cores A and B as functions of the propagation distance.

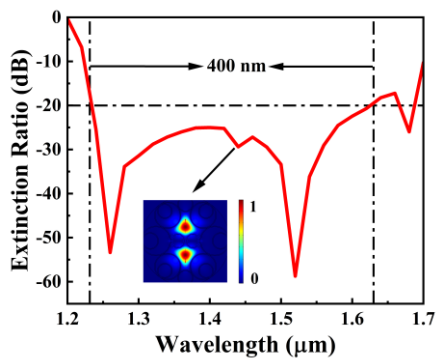

Fig. 13. The polarization *ER* as a function of wavelength, the insert showing the mode field distribution of the *y*-pol odd mode calculated at wavelength 1.44 μm.

When the length of the DHC-NCF PBS is 6.45 cm, the polarization *ER* as a function of wavelength is shown in Fig. 13. From Fig. 13, the polarization *ER*s of -53.4 dB and -58.8 dB are achieved at wavelengths 1.26 μm and 1.52 μm, respectively. In addition, there is a turning point at wavelength 1.44 μm, and the inset of Fig. 13 shows the mode field distribution of the *y*-pol odd mode at this turning point. From the inset, the two silica tubes in the middle are very close to each other, and the *y*-pol odd mode couples with the walls of the two silica tubes and a part of the energy leaks to the silica tube walls. And the polarization ER is below -20 dB in the wavelength range of 1.23 to 1.63 μm. Therefore, the proposed DHC-NCF PBS has a bandwidth of ~ 400 nm with the *ER* below -20 dB, covering the O+E+S+C+L communication band.

Fig. 14 shows the confinement losses of the modes LP_{01} and LP_{11} and HOMER as

functions of wavelength. From Fig. 14, the confinement loss of the mode LP_{01} always remains about 1 dB/m in the wavelength range of 1.35 to 1.62 μm, and the confinement loss of the mode LP_{11} is always higher than 1000 dB/m in the wavelength range of 1.20 to 1.70 μm. And the HOMER is larger than 100 in the wavelength of 1.23 to 1.7 μm, and reaches 1000 near wavelength 1.55 μm, which indicates that the proposed DHC-NCF PBS has good single-mode characteristics.

The proposed DHC-NCF PBS could be fabricated by the stack and draw technique [40]. First, the silica capillaries with different sizes are stacked according to the designed DHC-NCF structure, and then several short capillaries are inserted into the ends to support the long silica capillaries and the inner nested capillaries to avoid the position shift and stack collapse. Second, the preform is drawn into the desired DHC-NCF using the drawing tower at high temperature, and the air pressure inside the preform is controlled during the drawing to prevent the silica tubes from collapsing. Finally, the ends of the fabricated DHC-NCF are cut off, and only the desired middle portion is retained.

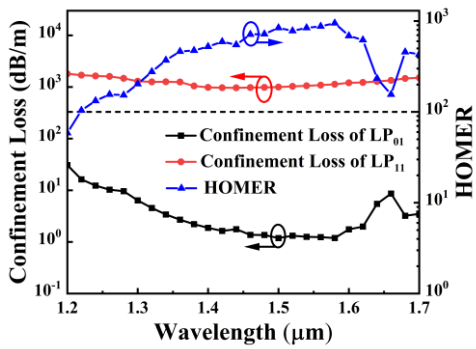

Fig. 14. The confinement losses of the modes LP_{01} and LP_{11} and HOMER in the wavelength range of 1.2 to 1.7 μm.

4. Conclusion

In conclusion, a broad bandwidth DHC-NCF PBS is proposed. The effects of the structure parameters of the DHC-NCF PBS are analyzed to obtain the *CLR* of ~ 0.5. The simulation results show that the polarization *ER* of the proposed DHC-NCF PBS can reach -53.4 dB and -58.8 dB at wavelengths 1.26 μm and 1.52 μm, respectively, and the maximum value of the HOMER can reach 948 at wavelength 1.58 μm. In the wavelength range of 1.23 to 1.63 μm, the polarization *ER* is less than -20 dB, and the HOMER is higher than 100. It means that the designed DHC-NCF PBS has good single-mode characteristics and a broad bandwidth of ~ 400 nm, covering the O+E+S+C+L communication band. It is believed that the proposed DHC-NCF PBS has important application in the optical communication system.

Funding

Natural Science Foundation of China (Granted No. 61935007).

Acknowledgements

We thank the State Key Laboratory of Information Photonics and Optical Communications (Beijing University of Posts and Telecommunications of China) for the scientific helps and supports throughout this research.

Disclosures

The authors declare no conflicts of interest.

References

1. K. Tan, Y. Huang, G. Q. Lo, C. Yu, and C. Lee, "Experimental realization of an O-band compact polarization splitter and rotator," Opt. Express 25, 3234-3241 (2017).
2. F.T. He, W. J. Shi, Z. Q. Hui, F. Zhan, and Y.K. Zhang, "A dual-core PCF polarization splitter with five elliptical air holes based on tellurite glass," Opt. Quant. Electron 49, 363 (2017).
3. M.F.O. Hameed, R.T. Balat, A.M. Heikal, M.M. Abo-Elkhier, M.I. Abo el Maaty and S.S.A. Obayya, "Polarization-Independent Surface Plasmon Liquid Crystal Photonic Crystal Multiplexer–Demultiplexer," IEEE Photon. J. 7(5), 1-10 (2015).
4. F.J. Tian, G.Y. Liu, J. F. Luo, C.Y. Yao, L. Li, X.H. Yang, and J.Z. Zhang, "A modified dual-core THz fiber polarization splitter with four subwavelength tubes," Optik 225, 162862 (2021).
5. L. Xu, Y. Wang, E. El-Fiky, D. Mao, A. Kumar, Z. Xing, M.G. Saber, M. Jacques, and D.V. Plant, "Compact Broadband Polarization Beam Splitter Based on Multimode Interference Coupler With Internal Photonic Crystal for the SOI Platform," J. Lightwave Technol. 37(4), 1231-1240(2019).
6. W.L. Lu, S.Q. Lou, X. Wang, L.W. Wang, and R.J. Feng, "Ultrabroadband polarization splitter based on three-core photonic crystal fibers," Appl. Opt. 52, 449-455 (2013).
7. Y.Y. Zhao, S.G. Li, X.Y. Wang, G.Y. Wang, M. Shi, and J.J. Wu, "Design of a novel multi channel photonic crystal fiber polarization beam splitter," Opt. Commun. 400, 79-83 (2017).
8. H.Y. Wang, X. Yan, S.G. Li, and X.N. Zhang, "Tunable surface plasmon resonance polarization beam splitter based on dual-core photonic crystal fiber with magnetic fluid," Opt. Quant. Electron. 49, 368 (2017).
9. N. Gómez-Cardona, C. Jiménez-Durango, J. Usuga-Restrepo, P. Torres, and E. Reyes-Vera, "Thermo-optically tunable polarization beam splitter based on selectively gold-filled dual-core photonic crystal fiber with integrated electrodes," Opt. Quant. Electron. 53, 68 (2021).
10. Y.X. Zhang, Y.W. Qu, J.H. Yuan, H.Y. Wang, X. Zhou, J.H. Huo, B.B. Yan, Q. Wu, K.R. Wang, K.P. Long, and C.X. Yu, "Polarization Beam Splitter Based on the Gold Wire-Filled Dual-Core Photonic Crystal Fiber at the Communication Wavelengths," Fiber and Integrated Opt. 40(1), 70-83(2021).
11. W. Zhou, J.C. Zhang, S.N. An, C. Liu, Y. Shi, J.W. Lv, L.Y. Yang, and P.K. Chu, "Dual-core photonic crystal fiber polarization beam splitter filled with salt water," Opt. Eng. 60(10), 106101 (2021).
12. H.Y. Wang, X. Yan, S.G. Li, G.W. An, and X.N. Zhang, "Ultra-short polarization beam splitter based on dual core photonic crystal fiber," J. Modern Opt. 64(5), 445-450 (2017).
13. J.S. Wang, L. Pei, S.J. Weng, L.Y. Wu, J. Li, and T.G. Ning, "Ultrashort polarization beam splitter based on liquid-filled dual-core photonic crystal fiber," Appl. Opt. 57, 3847-3852 (2018).
14. M.T. Rahman and A. Khaleque, "Ultra-short polarization splitter based on a plasmonic dual-core photonic crystal fiber with an ultra-broad bandwidth," Appl. Opt. 58, 9426-9433 (2019).
15. D. Bird, "Attenuation of model hollow-core, anti-resonant fibres," Opt. Express 25, 23215-23237 (2017).
16. X. Chen, X.W. Hu, L.Y. Yang, J.G. Peng, H.Q. Li, N.L. Dai, and J.Y. Li, "Double negative curvature anti-resonance hollow core fiber," Opt. Express 27, 19548-19554 (2019).
17. A. Deng, I. Hasan, Y.X. Wang, and W. Chang, "Analyzing mode index mismatch and field overlap for light guidance in negative-curvature fibers," Opt. Express 28, 27974-27988 (2020).
18. W. Belardi and J.C. Knight, "Effect of core boundary curvature on the confinement losses of hollow antiresonant fibers," Opt. Express 21, 21912-21917 (2013).
19. C. Subhasis, V.P. Lieke, P. Francesco, S. Pier, "Low loss transmission in negative curvature optical fibers with elliptical capillary tubes," J. Lightwave Technol. 34(18), 4228-4231 (2016).
20. A.N. Kolyadin, G.K. Alagashev, A.D. Pryamikov, L. Mouradian, A. Zeytunyan, H. Toneyan, A.F. Kosolapov, I.A. Bufetov, "Negative Curvature Hollow-core Fibers: Dispersion Properties and Femtosecond Pulse Delivery," Phys. Procedia 73, 59-66 (2015).
21. Z.X. Liu, K. B. Petrov, G. Lidia, H. John. R., L. Domanic, C. Kari, T. B. Charles, S. Kai, E. Daniel, P. Marco, R. David J., P. Francesco, S. Radan, B. Polina, "Nonlinearity-free Coherent Transmission in Hollow-Core Antiresonant Fiber," J. Lightwave Technol. 37(3), 909-916 (2019).
22. C.L. Wei, J. T. Young, C. R. Menyuk, and J. Hu, "Temperature sensor based on liquid-filled negative curvature optical fibers," OSA Continuum. 2, 2123-2130 (2019).
23. F. Yu, W.J. Wadsworth, and J.C. Knight, "Low loss silica hollow core fibers for 3–4 μm spectral region," Opt. Express 20, 11153-11158 (2012).
24. M.S. Habib, C. Markos, J. E. Antonio-Lopez, and R. Amezcua-Correa, "Multioctave supercontinuum from visible to mid-infrared and bend effects on ultrafast nonlinear dynamics in gas-filled hollow-core fiber," Appl. Opt. 58, D7-D11 (2019).
25. C.L. Wei, C.R. Menyuk, and J. Hu, "Polarization-filtering and polarization-maintaining low-loss negative curvature fibers," Opt. Express 26, 9528-9540 (2018).
26. A.V. Gladyshev, A.N. Kolyadin, A.F. Kosolapov, Y.P. Yatsenko, A.D. Pryamikov, A.S. Biriukov, I.A. Bufetov, and E.M. Dianov, "Low-threshold 1.9 μm Raman generation in microstructured hydrogen-filled hollow-core revolver fibre with nested capillaries," Laser Phys. 27(2), 025101 (2016).

27. S.O. Leonov, E.A. Yelistratova, V.V. Demidov, and A.D. Pryamikov, “Birefringence properties of anti-resonant octagonal-core and nodeless hollow-core fibers,” Appl. Opt. 59, 5013-5019 (2020).
28. X.S. Huang, J. Ma, D.Y. Tang, and S. Yoo, “Hollow-core air-gap anti-resonant fiber couplers,” Opt. Express 25, 29296-29306 (2017).
29. T.T. Zhao, H.Q. Jia, Z.G. Lian, T. Benson, S.Q. Lou, “Ultra-broadband dual hollow-core anti-resonant fiber polarization splitter,” Opt. Fiber Technol. 53(102005), 1068-5200 (2015).
30. H.Q. Jia, X. Wang, T.M. Benson, S. Gu, S.Q. Lou, and X.Z. Sheng, “Ultrawide bandwidth dual sakura hollow-core antiresonant fiber polarization beam splitter,” J. Opt. Soc. Am. B 38, 3395-3402 (2021).
31. H.Q. Jia, X. Wang, T.T. Zhao, Z.J. Tang, Z.G. Lian, S.Q. Lou, and X.Z. Sheng, “Ultrawide bandwidth single-mode polarization beam splitter based on dual-hollow-core antiresonant fiber,” Appl. Opt. 60(31), 9781–9789, (2021).
32. K.S.R. Shaha, A. Khaleque, M.T. Rahman, and M.S. Hosen, “Broadband and Short-Length Polarization Splitter on Dual Hollow-Core Antiresonant Fiber,” IEEE Photon. Technol. Lett. 34(5), 259-262, (2022).
33. S. Qiu, J.H. Yuan, X. Zhou, F. Li, Q.W. Wang, Y.W. Qu, B.B. Yan, Q. Wu, K.R. Wang, X.Z. Sang, K.P. Long, and C.X. Yu, “Hollow-Core Negative Curvature Fiber with High Birefringence for Low Refractive Index Sensing Based on Surface Plasmon Resonance Effect,” Sensors 20, 6539 (2020).
34. S.S. Li, H. Zhang, Y. Hou, J.J. Bai, W.W. Liu, and S.J. Chang, “Terahertz polarization splitter based on orthogonal microstructure dual-core photonic crystal fiber,” Appl. Opt. 52, 3305-3310 (2013).
35. Q. Xu, Y. Zhao, H.P. Xia, S.B. Lin, Y.N. Zhang, “Ultrashort polarization splitter based on dual-core photonic crystal fibers with gold wire,” Opt. Eng. 57(4), 046104.
36. C.L. Wei, R.A. Kuis, F. Chenard, C.R. Menyuk, and J. Hu, “Higher-order mode suppression in chalcogenide negative curvature fibers,” Opt. Express 23, 15824-15832 (2015).
37. Y.W. Qu, J.H. Yuan, X. Zhou, F. Li, B.B. Yan, Q. Wu, K.R. Wang, X.Z. Sang, K.P. Long, and C.X. Yu, “Surface plasmon resonance-based silicon dual-core photonic crystal fiber polarization beam splitter at the mid-infrared spectral region,” J. Opt. Soc. Am. B 37, 2221-2230 (2020).
38. V. Kumar, R. K. Varshney, and S. Kumar, “Design of a compact and broadband terahertz polarization splitter based on gradient dual-core photonic crystal fiber,” Appl. Opt. 59, 1974-1979 (2020).
39. Z.H. Zhang, Y.F. Shi, B.M. Bian, and J. Lu, “Dependence of leaky mode coupling on loss in photonic crystal fiber with hybrid cladding,” Opt. Express 16, 1915-1922 (2008).
40. F. Yu, J.C. Knight, “Negative Curvature Hollow-Core Optical Fiber,” IEEE J. Sel. Top. Quantum Electron. 22, 146–155 (2016).